The Astrophysical Journal, 622:319–332, 2005 March 20

STARS IN THE HUBBLE ULTRA DEEP FIELD

N. Pirzkal,[1] K. C. Sahu,[1] A. Burgasser,[2] L. A. Moustakas,[1] C. Xu,[1] S. Malhotra,[1] J. E. Rhoads,[1]
A. M. Koekemoer,[1] E. P. Nelan,[1] R. A. Windhorst,[3] N. Panagia,[1] C. Gronwall,[4]
A. Pasquali,[5] and J. R. Walsh[6]

Received 2004 September 29; accepted 2004 December 3

ABSTRACT

We identified 46 unresolved source candidates in the Hubble Ultra Deep Field (HUDF) down to $i_{775} = 29.5$. Unresolved objects were identified using a parameter *S*, which measures the deviation from the curve of growth of a point source. Extensive testing of this parameter was carried out, including the effects of decreasing signal-to-noise ratio and of the apparent motions of stars, which demonstrated that stars brighter than $i_{775} = 27.0$ could be robustly identified. Low-resolution grism spectra of the 28 objects brighter than $i_{775} = 27.0$ identify 18 M and later stellar type dwarfs, two candidate L dwarfs, two QSOs, and four white dwarfs. Using the observed population of dwarfs with spectral type M4 or later, we derive a Galactic disk scale height of 400 ± 100 pc for M and L stars. The local white dwarf density is computed to be as high as $(1.1 \pm 0.3) \times 10^{-2}$ stars pc^{-3}. On the basis of observations taken 73 days apart, we determined that no object in the field has a proper motion larger than $0\farcs027$ yr^{-1} (3 σ detection limit). No high-velocity white dwarfs were identified in the HUDF, and all four candidates appear more likely to be part of the Galactic thick disk. The lack of detected halo white dwarfs implies that if the dark matter halo is 12 Gyr old, white dwarfs account for less than 10% of the dark matter halo mass.

Subject headings: Galaxy: disk — Galaxy: stellar content — Galaxy: structure — stars: late-type — white dwarfs

Online material: color figures

1. INTRODUCTION

Studying the stellar content of our galaxy down to the faintest possible magnitudes is necessary to study the structures of the Galactic disk and Population II halo (referred to as the Galactic halo hereafter) and stellar population (Méndez et al. 1996). The nature of the Galactic dark matter halo has in addition been the subject of some debate since the MACHO project (Alcock et al. 2000) observed lensing events in the direction of the Large Magellanic Cloud and claimed that 20% of the dark matter halo mass could be in the form of low-mass objects with masses smaller than 1.0 $M_\odot$ (Alcock et al. 2000). Although there are alternative explanations for the observed lensing events (Sahu 1994, 2003; Gates & Gyuk 2001 and references therein), the detection of faint, blue unresolved objects with high proper motion has been used as evidence for the existence of a large population of old white dwarfs in the Galactic dark matter halo. Oppenheimer et al. (2001) estimated that about 2% of the dark matter halo mass could be accounted for by old halo white dwarfs. There has since been some debate as to whether the former result might have been caused by a dynamically warmer thick disk component (Reid et al. 2001) and the latter might have been affected by the misidentification of faint blue extragalactic sources (Kilic et al. 2004; see also Reid 2005 for a complete review). The existence of ultracool white dwarfs ($T \leq 4000$ K), however, has been confirmed in recent Sloan Digital Sky Survey (SDSS) data (Gates et al. 2004).

A search for distant white dwarfs using deeper observations provides another opportunity to firmly examine the existence of a significant population of old white dwarfs in the Galactic halo and the dark matter halo. As shown by Kawaler (1996), deep broadband imaging can probe a significant portion of the Galactic dark matter halo and should identify Galactic dark matter halo white dwarfs in the process. Ideally, one would like to identify white dwarf candidates spectroscopically, instead of relying on broadband colors only, and to determine their Galactic disk or halo memberships using sensitive proper-motion measurements.

The Advanced Camera for Survey (ACS) *Hubble Space Telescope* (*HST*) observations of the Hubble Ultra Deep Field (HUDF; S. Beckwith et al. 2005, in preparation) and their unprecedented depths offer a new opportunity to detect faint stars, such as white dwarfs, at high Galactic latitude. Additionally, the Grism ACS Program for Extragalactic Science (GRAPES) survey (PI: S. M.; see description in Pirzkal et al. 2004) provides low-resolution spectra of most sources in the HUDF. These spectra can be used to confidently determine spectral types of stars in the HUDF down to $i_{775} = 27.0$ mag. More importantly, these spectra allow one to differentiate unresolved blue, faint extragalactic objects (e.g., QSOs) from white dwarfs and other stars.

Section 3 outlines how unresolved sources were identified in the HUDF, whereas the spectroscopic identification of unresolved sources is discussed in § 4. Section 5 describes an analysis of the cumulative number distribution of the late-type dwarfs identified in the HUDF and its implication for the Galactic disk

[1] Space Telescope Science Institute, 3700 San Martin Drive, Baltimore, MD 21218.
[2] Department of Astrophysics, American Museum of Natural History, Central Park West at 79th Street, New York, NY 10024; adam@amnh.org.
[3] Department of Physics and Astronomy, Arizona State University, Box 871504, Tempe, AZ 85287-1504.
[4] Department of Astronomy and Astrophysics, Pennsylvania State University, 525 Davey Laboratory, University Park, PA 16802.
[5] Institute of Astronomy, ETH Zürich Hönggerberg, CH-8093 Zurich, Switzerland.
[6] ESO/ST-ECF, Karl-Schwarschild-Strasse 2, Garching bei München D-85748, Germany.

structure (§ 5.1). Section 5 also includes a description of the white dwarf content of the Galactic disk and halo (§ 5.2).

2. DESCRIPTION OF THE DATA

The HUDF was imaged using the ACS and the F435W (B_{435}), F606W (V_{606}), F775W (i_{775}), and F850LP (z_{850}) bands at different epochs. The observations were carried out by cycling through each filter while using a small dither pattern to mask out the ACS interchip gap and other cosmetic problems. The HUDF was observed during four different visits, rotating the field of view to a different position angle each time (0°, 8°, 85°, and 91° with respect to the first visit; S. Beckwith et al. 2005, in preparation). The individual ACS images had an integration time of 1200 s, a size of 4096 pixels × 4096 pixels, and a pixel scale of 0.″050 pixel^{-1}. These images were combined by drizzling them onto a finer pixel grid with a pixel scale of 0.″030 pixel^{-1} while geometrically correcting these images. The limiting AB magnitudes (signal-to-noise ratio of 10) of the i_{775} and z_{850} images are 29.0 and 28.7 mag, respectively. In this paper, images taken from 2003 September 24 to October 28 and from 2003 December 4 to 2004 January 15 are referred to as epoch 1 and 2 images, respectively. The elapsed time between the mean observing dates of the two epochs is 73 days. Images from epoch 1 and epoch 2 were taken at position angles that are nearly 90° apart.

Whereas the deep, combined ACS HUDF images described above were used to determine which objects are unresolved (§ 3), eight special partial image stacks were also assembled to take advantage of the fact that the data were taken over a period of several months. Four partial image stacks were created for each HUDF epoch, using exactly the same method used to create the original combined HUDF images. These partial image stacks can be used to determine the variability (S. Cohen et al. 2005, in preparation), as well as measure the proper and parallax motions of the objects in the field. The eight partial image stacks have the same physical properties as the combined ACS HUDF images but with one-eighth of the integration time. Note that the cosmic-ray rejection step was done separately while assembling each partial image stack so that any strongly varying or moving object would not be removed by the cosmic-ray rejection process. The astrometric registration of the combined HUDF images and the eight partial image stacks is estimated to be better than 0.1 ACS pixels (0.″005, or 0.16 HUDF image pixels; S. Beckwith et al. 2005, in preparation).

Spectroscopic observations of the HUDF using the ACS slitless grism mode (G800L) were carried out as part of the GRAPES project. The reader is referred to Pirzkal et al. (2004) for an in-depth description of these spectra. These spectra are low-resolution spectra ($R = 100$), span a wavelength range of 5500 Å $\leq \lambda \leq$ 10500 Å, and can be used to spectroscopically identify objects in the field.

The HUDF Public Catalog 1.0, containing 10,181 objects, was used to identify objects in the field, and all objects are referred to by their ID in this catalog ("UID"). The magnitudes of these objects were remeasured using matched aperture photometry with apertures defined using SExtractor (Bertin & Arnouts 1996) and the i_{775}-band HUDF image. The photometric ACS magnitude zero points (25.65288, 26.49341, 25.64053, and 24.84315 in the B_{435}, V_{606}, i_{775}, and z_{850} bands, respectively) were taken from the GOODS survey (Giavalisco et al. 2004).

3. IDENTIFICATION OF POINT SOURCES IN THE HUDF

We identified unresolved objects in the HUDF using a single-index (S) method that is based on a simple analysis of the curve

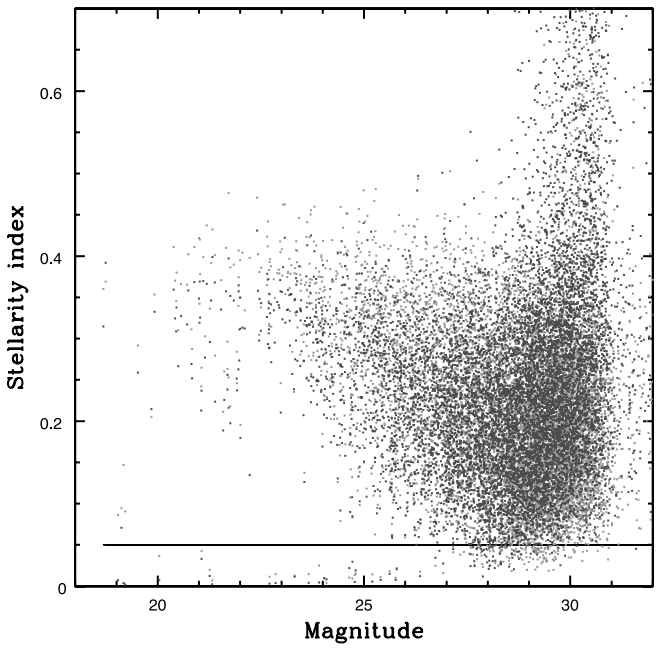

FIG. 1.—Distribution of $S_{i_{775}}$ (*light gray*) and $S_{z_{850}}$ (*dark gray*) values for the 10,181 HUDF objects. The stellarity index S was defined (see § 3) so that higher values correspond to objects that are increasingly resolved in the images. We selected unresolved objects fainter than $i_{775} \geq 20.0$ mag to be unresolved if $S_{z_{850}} \leq 0.05$, and $S_{z_{850}} \leq 0.15$ for brighter objects, which are saturated. [*See the electronic edition of the Journal for a color version of this figure*.]

of growth of the light distribution of an object. The IRAF task RADPROF was used to produce these light curves of growth. This task first computes the intensity-weighted center of the object (in a 3 pixel × 3 pixel box) and then performs aperture photometry using increasing aperture sizes (up to a radius of 10 pixels). These photometric measurements are then fitted (using eight 3 σ rejection cycles) to a cubic spline of order 5. RADPROF was applied to stamp images of objects that were masked using SExtractor segmentation maps. These segmentation maps were used to avoid contamination from neighboring objects. The RADPROF parameters described here were selected because, following extensive initial testing, they were found to result in curves of growth that are not too sensitive to the presence of faint nearby objects while consistently remaining sensitive to the presence of faint, diffuse extended emission around objects. The stellarity S of an object is defined as

$$S^2 = \frac{1}{r_{\max}} \sum_{r=0}^{r_{\max}} \left[F_{\rm obj}(r) - F_{\rm psf}(r) \right]^2,$$

where $F_{\rm obj}(r)$ and $F_{\rm psf}(r)$ denote the curve of growth of light, normalized to 1.0 at a distance of $r_{\max}$, of the object and of a point source. A value of 10 was used for $r_{\max}$.

The index S is then simply the square root of the sum of the squared differences between the two curves. Unresolved objects have S-values that are close to 0.0, whereas increasingly resolved objects produce increasingly larger (unbound) values of S. The detailed calibration of S was done in several stages, each time refining the reference curve of growth that was used. This is described in some detail below.

First, a few obvious, bright, unresolved, and unsaturated sources were preselected for further study. This was done in both the i_{775}- and the z_{850}-band images separately. The GRAPES

TABLE 1
UNRESOLVED OBJECTS IN THE HUDF

UID	R.A. (J2000.0) (deg)	Decl. (J2000.0) (deg)	B_{435}	$B_{435}-V_{606}$	$V_{606}-i_{775}$	$i_{775}-z_{850}$	$S_{i_{775}}$	$S_{z_{850}}$
19	53.1623248	−27.8269460	26.58	1.91	1.01	0.30	0.015	0.004
366	53.1753062	−27.8198904	29.99	2.20	3.05	1.27	0.009	0.030
443	53.1583988	−27.8189953	31.25	0.86	3.47	1.51	0.016	0.028
834	53.1648156	−27.8143652	27.67	2.35	2.00	0.76	0.013	0.011
911	53.1460739	−27.8123237	25.21	2.09	1.80	0.65	0.007	0.002
1147	53.1834639	−27.8067589	19.58	−0.16	0.52	0.13	0.091	0.002
1343	53.1398080	−27.8100295	27.36	−0.23	−0.14	−0.04	0.045	0.046
2150	53.1767483	−27.7996684	22.60	1.99	1.43	0.80	0.147	0.003
2368	53.1676057	−27.8037923	29.07	1.18	0.08	−0.20	0.046	0.050
2457	53.1616105	−27.8027738	26.98	1.91	0.98	0.30	0.004	0.008
2977	53.1726388	−27.8006672	27.94	−0.18	−0.21	0.18	0.042	0.049
3166	53.1583425	−27.7949215	20.80	0.96	0.80	0.37	0.086	0.007
3561	53.1483050	−27.7977856	29.24	1.98	0.91	0.24	0.018	0.012
3794	53.1474097	−27.7965561	28.89	2.14	0.98	0.29	0.010	0.007
3940	53.1498728	−27.7961691	27.06	−0.48	−0.21	−0.18	0.033	0.038
4120	53.1839107	−27.7954147	28.04	0.03	0.12	1.31	0.023	0.012
4322	53.1349058	−27.7944480	26.83	0.06	−0.06	−0.07	0.067	0.043
4643	53.1848922	−27.7933971	31.73	1.52	0.74	0.25	0.019	0.050
4839	53.1883621	−27.7923200	27.22	1.20	0.40	0.07	0.018	0.015
4945	53.2003709	−27.7898451	25.06	2.06	1.74	0.67	0.020	0.013
5317	53.1257144	−27.7904647	29.06	0.49	−0.00	−0.30	0.045	0.039
5441	53.1625253	−27.7896458	27.81	1.75	1.27	0.39	0.016	0.019
5921	53.1322881	−27.7828516	20.57	0.77	1.19	0.51	0.094	0.070
5992	53.1498432	−27.7874448	27.52	1.63	0.69	0.16	0.014	0.005
6334	53.1782000	−27.7861688	27.71	−0.27	−0.16	−0.18	0.049	0.049
6442	53.1416300	−27.7856726	28.16	−0.19	0.04	−0.07	0.044	0.030
6461	53.1984259	−27.7848674	26.80	1.77	1.00	0.30	0.010	0.010
6620	53.1428439	−27.7849376	31.27	3.19	0.25	−0.14	0.041	0.049
6732	53.1784892	−27.7840395	25.73	1.13	−0.04	0.01	0.010	0.022
7113	53.1707114	−27.7826303	30.83	2.49	0.65	0.20	0.026	0.024
7194	53.1860335	−27.7822207	26.91	−0.12	−0.13	−0.06	0.048	0.045
7357	53.1692789	−27.7813943	27.93	0.10	−0.21	−0.16	0.024	0.031
7525	53.1318579	−27.7820076	28.70	2.22	1.08	0.30	0.011	0.007
7768	53.1472186	−27.7714786	27.12	1.66	0.68	0.20	0.014	0.005
7894	53.1831085	−27.7802451	27.46	0.03	−0.15	−0.12	0.047	0.039
8081	53.1580838	−27.7701503	27.92	−0.32	−0.40	−0.30	0.038	0.020
8157	53.1649526	−27.7736713	30.85	2.16	0.40	0.07	0.042	0.039
8186	53.1867094	−27.7735490	27.72	−0.13	−0.14	−0.34	0.044	0.029
9006	53.1853179	−27.7799976	27.46	−0.05	−0.07	0.24	0.039	0.024
9020	53.1685421	−27.7805214	27.00	0.28	−0.01	−0.16	0.025	0.034
9212	53.1485421	−27.7701387	25.50	1.82	0.96	0.29	0.011	0.003
9230	53.1580164	−27.7691869	21.18	0.76	0.38	0.10	0.037	0.007
9331	53.1638484	−27.767128	27.95	2.20	1.84	0.67	0.025	0.005
9351	53.1781506	−27.7691241	26.21	2.03	1.32	0.42	0.015	0.004
9397	53.162852	−27.7671662	21.44	0.26	0.11	0.02	0.043	0.033
9959	53.1611698	−27.7555109	29.12	2.42	0.91	0.29	0.022	0.021

NOTE.—Objects were selected using the criterion that $S_{i_{775}}$ and $S_{z_{850}} \leq 0.05$ mag (F850LP ACS band).

spectra of these sources were examined, and a main-sequence star was selected (UID 911). The curves of growth of this object were measured separately in the i_{775} and z_{850} bands and were used to compute $S_{i_{775}}$ and $S_{z_{850}}$ values for all 10,181 objects in the HUDF. A new set of 25 bright point sources, well distributed over the whole ACS field, were then carefully selected on the basis of their low $S_{z_{850}}$ values (arbitrarily chosen to be $S_{z_{850}} \leq 0.04$). The GRAPES spectra of these 25 objects were visually inspected to ensure that these objects were stars. Stamp images of these objects were individually drizzled (Fruchter & Hook 2002) and carefully recentered to produce a stack of images, which were then combined to produce empirical i_{775} and z_{850} point-spread function (PSF) images. A sigma-based rejection algorithm was used to avoid the effect of any faint neighbor in the final combined images. Final i_{775}- and z_{850}-band reference curves of growth were generated using these empirical PSF estimates, and all of the $S_{i_{775}}$ and $S_{z_{850}}$ values were recomputed. Figure 1 shows the distributions of the S-values in both the i_{775} and z_{850} bands as a function of magnitude. There are clearly two distinct groups of object in the HUDF images. One group consists of objects that are completely or partially resolved, forming a large distribution around the S-value of 0.2 and $i_{775} = 28.0$ mag. A second group consists of unresolved objects with low S-values at all magnitudes. Bright stars in Figure 1 are observed to have S-values that are consistently lower than 0.05. The exceptions are bright stars near $i_{775} = 18$ mag, which are saturated and have artificially high values of S ($\approx$0.1). The effect of bright-star saturation on the measured values of S were investigated, and

values of $0.1 \leq S \leq 0.15$ are expected if the center of a star is saturated or missing in the HUDF images. Nevertheless, the populations of resolved and unresolved objects appear to be well separated at brighter magnitudes in Figure 1.

Unresolved sources in the HUDF were selected using the criterion that $S_{z_{850}}$ and $S_{i_{775}} \leq 0.05$ mag. Five bright saturated stars were manually added to the final object list. The final list of unresolved HUDF sources contains 46 objects, spanning the magnitude ranges of $19.0 \leq i_{775} \leq 29.5$ and $18.3 \leq z_{850} \leq 29.2$. Table 1 summarizes some of the properties of these objects.

3.1. *Testing the Selection Process*

The ability to distinguish between resolved and unresolved objects using *S*-values was extensively tested, using a subset of the HUDF object catalog containing the 369 brightest ($z_{850} \leq 25.0$ mag) objects in the field. Simulated i_{775}- and z_{850}-band images of these objects, made 0.0, 0.75, 2.0, 3.0, 4.0, 5.0, 6.0, 7.0, 8.0, and 9.0 mag fainter, were created and *S*-values measured using each simulated image, exactly as described in § 3. The *S*-value of each of these 369 test objects was thus measured 10 times, each measurement corresponding to a different apparent magnitude. Figure 2 shows how the *S*-value remains largely unchanged as an object is made fainter and noisier, all the way down to $i_{775} = 29.0$ mag. The vertical pattern seen in this figure is a result of the 10 magnitude steps used in this simulation. This test demonstrates a very small fraction of misclassification: not a single extended object was misclassified as a star (e.g., no object with $S \geq 0.05$ originally in the HUDF images was measured to have $S \leq 0.05$ as the object was made fainter), and fewer than 5% of stars were misclassified down to $i_{775} = 29.0$ mag. Although some objects shown in Table 1 are fainter than this, only objects significantly brighter than this limit ($i_{775} \leq 27.0$ mag) are actually included in the analysis described below, and these are expected to be bona fide unresolved objects.

3.2. *Testing the Effect of Proper Motion*

Some of the stars among the HUDF objects could have a high tangential velocity (V_t) and a correspondingly large proper motion. Such objects would be blurred in the combined HUDF images and would appear to be resolved. Similarly, nearby objects would suffer from a significant amount of parallax, again causing these objects to be blurred and misidentified. The index *S* proved relatively insensitive to a small amount of object motion. This is not unexpected, since *S* was tuned to the detection of faint extended components. The curves of growth produced by RADPROF were computed by summing, using several sigma-rejection steps, the pixel intensities inside annuli of increasing radii. The effect of a nearby source is strongly diminished as its separation from the main source increases and the number of unaffected pixels increases. In addition, the use of a fifth-order spline imposes some smoothness on the curve of growth, which further lowers the effect of a nearby object. Still, the effect of object motion on measured values of *S* was carefully investigated by generating images of the 46 unresolved HUDF objects that were selected as described in § 3. These were appropriately shift-and-added, accounting for the orientation and pointing used for each individual HUDF observation while allowing objects to move as a function of time, to simulate the effect of proper motion. As larger values of proper motion were introduced, the *S*-values increased only slightly, and *S* was found to be mostly unaffected by shifts smaller than 2.5 HUDF pixels ($\mu = 0\farcs3\ \mathrm{yr}^{-1}$). In fact, 70% of objects were still properly identified as point sources when shifts of 2.5 and 5.0 HUDF pixels were applied ($0.3 \leq \mu \leq 0.6$).

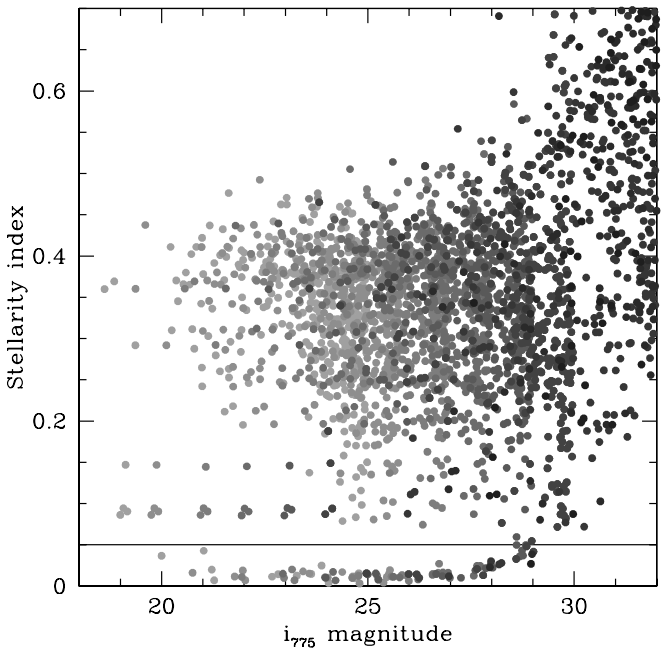

FIG. 2.—Distribution of $S_{z_{850}}$ values for the brightest 369 objects in the field. Each object appears 10 times in this figure, with increasingly lower signal-to-noise ratio (*increasingly darker circles*). The observed increase in *S*-values as a function of magnitude at $i_{775} \geq 29.0$ mag is similar to the one observed in Fig. 1, where the real distribution of the *S*-values from the 10,181 HUDF objects is shown. This demonstrates the robustness of *S* to distinguish between point sources and extended objects down to faint magnitudes. At fainter magnitudes, images of stars become increasingly dominated by noise, which tends to increases the measured values of *S*. The same test was performed in the i_{775} band and yielded identical behavior. [*See the electronic edition of the Journal for a color version of this figure*.]

4. IDENTIFYING STARS

4.1. *Using Grism Spectra to Identify Stars*

The spectral type of 28 unresolved objects brighter than $i_{775} = 27.0$ could be determined robustly using template fitting of their GRAPES spectra (Pirzkal et al. 2004). The template set included Pickles (1998) main-sequence templates, L and T dwarf spectra (Kirkpatrick et al. 2000; Burgasser et al. 2003), DA and DB white dwarf spectra (Harris et al. 2003) obtained from the SDSS archive, and some low-temperature (3000, 5000, and 8000 K) model spectra of white dwarfs (Harris et al. 2001). The quality of each spectral fit was evaluated visually, and the results of these fits are given in Table 2. Objects too faint to have reliable fits are indicated. The GRAPES spectra and the two best fits listed in Table 2 are shown in Figures 3, 4, and 5. Unresolved extragalactic sources are labeled as GAL in Table 2 and are discussed in more details in § 4.3.

Of the 46 point sources detected in the HUDF, 26 stars, all brighter than $i_{775} = 27.0$ mag, were identified. As shown in Table 2, the majority of stars in the HUDF (18 out of 26) are found to be M dwarfs. Figures 6 and 7 show these objects in V_{606} versus $B_{435} - V_{606}$ and i_{775} versus $V_{606} - i_{775}$ plots. Such plots have in the past shown a lack of faint red objects in the region $V_{606} \geq 27.0$ mag and $B_{435} - V_{606} \geq 1.0$ (Méndez et al. 1996). Objects found in this region of the plot appear to be either extragalactic or L-type dwarf spectra (e.g., UID 443 and UID 366). Further NIR observations will be required to verify

TABLE 2

Spectral Types and Distance Estimates of the Unresolved Objects in the HUDF

UID	Sp. Type	$i_{775} \geq 27.0$	$M_{V_{606}}$	log D		
				MS	WD $M_V = 14$	WD $M_V = 17$
19	M1–M2	No	9.30 ± 0.25	4.072 ± 0.050	3.129	2.529
366	L0–L1	No	18.9 ± 0.50	2.780 ± 0.100	3.750	3.150
443	L0–M6	No	15.6 ± 2.9	4.261 ± 0.570	4.274	3.674
834	M4–M5	No	11.4 ± 0.39	3.777 ± 0.077	3.258	2.658
911	M4–M5	No	11.4 ± 0.39	3.338 ± 0.077	2.818	2.218
1147	F6–F8	No	3.82 ± 0.17	4.180 ± 0.033	2.142	1.542
1343	A0–K7	Yes	4.32 ± 3.58	6.080 ± 0.716	3.713	3.113
2150	M3–M4	No	11.3 ± 0.23	2.862 ± 0.045	2.315	1.715
2368	O9–M6	Yes	4.19 ± 8.55	7.145 ± 1.710	3.774	3.174
2457	M0–M1	No	8.77 ± 0.28	4.258 ± 0.056	3.209	2.609
2977	A0–M4	Yes	11.28 ± 0.23	4.365 ± 0.045	3.818	3.218
3166	K4–K5	No	6.96 ± 0.14	3.573 ± 0.027	2.164	1.564
3561	M0–M1	No	8.77 ± 0.28	4.697 ± 0.056	3.647	3.047
3794	M0–M1	No	8.77 ± 0.28	4.594 ± 0.056	3.544	2.944
3940	O5–M3	Yes	2.37 ± 7.94	7.315 ± 1.588	3.702	3.102
4120	GAL	Yes	...	...	...	...
4322	A7–K5	No	4.70 ± 2.4	5.632 ± 0.479	3.548	2.948
4643	A0–M6	Yes	6.75 ± 5.96	6.578 ± 1.191	4.237	3.637
4839	G5–K2	No	5.65 ± 0.61	5.087 ± 0.122	3.400	2.800
4945	M4–M5	No	11.4 ± 0.38	3.315 ± 0.077	2.796	2.196
5317	A0–M6	Yes	6.71 ± 6.0	6.267 ± 1.199	3.910	3.310
5441	M2–M3	No	9.93 ± 0.38	4.228 ± 0.076	3.407	2.807
5921	K4–K5	No	6.96 ± 0.14	3.565 ± 0.027	2.155	1.555
5992	K7–M0	No	8.07 ± 0.43	4.568 ± 0.085	3.373	2.773
6334	F8–L0	Yes	8.34 ± 4.4	5.505 ± 0.875	3.791	3.191
6442	A0–G5	Yes	2.89 ± 2.2	6.271 ± 0.429	3.865	3.265
6461	M0–M1	No	8.77 ± 0.28	4.251 ± 0.056	3.202	2.602
6620	B8–M4	Yes	5.45 ± 5.6	6.345 ± 1.121	3.812	3.212
6732	GAL	No	...	...	...	...
7113	G8–K0	Yes	5.60 ± 0.19	5.543 ± 0.038	3.861	3.261
7194	O5–K5	Yes	0.76 ± 6.3	7.215 ± 1.266	3.601	3.001
7357	O9–M5	Yes	3.73 ± 8.1	7.131 ± 1.618	3.760	3.160
7525	M1–M2	No	9.33 ± 0.23	4.429 ± 0.045	3.491	2.892
7768	K5–K7	No	7.37 ± 0.27	4.616 ± 0.055	3.286	2.686
7894	B8–K7	Yes	3.73 ± 3.9	6.223 ± 0.780	3.680	3.080
8081	O5–A3	Yes	−1.98 ± 3.6	7.471 ± 0.716	3.843	3.243
8157	GAL	Yes	...	...	...	...
8186	B0–K7	Yes	1.89 ± 5.8	7.038 ± 1.151	3.764	3.164
9006	B9–A3	Yes	0.94 ± 0.65	6.328 ± 0.131	3.697	3.097
9020	F0–F2	No	3.16 ± 0.44	5.716 ± 0.089	3.540	2.940
9212	M0–M1	No	8.77 ± 0.28	3.979 ± 0.056	2.929	2.329
9230	K2–K3	No	6.40 ± 0.14	3.800 ± 0.028	2.279	1.679
9331	M5–M6	No	12.3 ± 0.45	3.701 ± 0.089	3.345	2.745
9351	M1–M2	No	9.30 ± 0.25	3.974 ± 0.050	3.031	2.431
9397	GAL	No	...	...	...	...
9959	M0–M1	No	8.77 ± 0.28	4.585 ± 0.056	3.535	2.935

Notes.—Of these objects, 28 are brighter than $i_{775} = 27.0$ mag. Their distance estimates assume that they are main-sequence objects or white dwarfs with $M_V = 14$ or 17. Two additional, fainter extragalactic sources are included (UIDs 4120 and 8157). The spectral types were determined by fitting the GRAPES (Pirzkal et al. 2004) spectra of these sources to a set of templates (see § 4.1).

the nature of these two L dwarf candidates by confirming that they both have the expected blue NIR colors of this type of object.

The HUDF field is at high Galactic latitude ($b = 223^\circ$, $l = -54^\circ$), and the effects of extinction and reddening are small ($A_V = 0.026$; Schlegel et al. 1998). The distances to the HUDF stars, which are shown in Table 2, were determined using their observed V_{606} magnitudes, their estimated stellar types, and the dwarf star main-sequence absolute Johnson V magnitudes from Allen (2000). The latter were converted to the V_{606} filter bandpass and AB magnitudes to be consistent with the data at hand. Distance estimates obtained under the assumption that these objects are white dwarfs with intrinsic magnitudes of $M_V = 14.0$ and 17.0 are also given.

4.2. *Proper-Motion Measurements*

The Galactic halo is isotropic and has no or little overall rotation. Halo objects are therefore expected to lag behind the rapidly rotating Galactic disk component (and the local standard of rest) with an average velocity of $\approx 200 \pm 100$ km s^{-1}. As done in Oppenheimer et al. (2001), it is assumed here that Galactic halo objects have a velocity that is more than 2 σ above

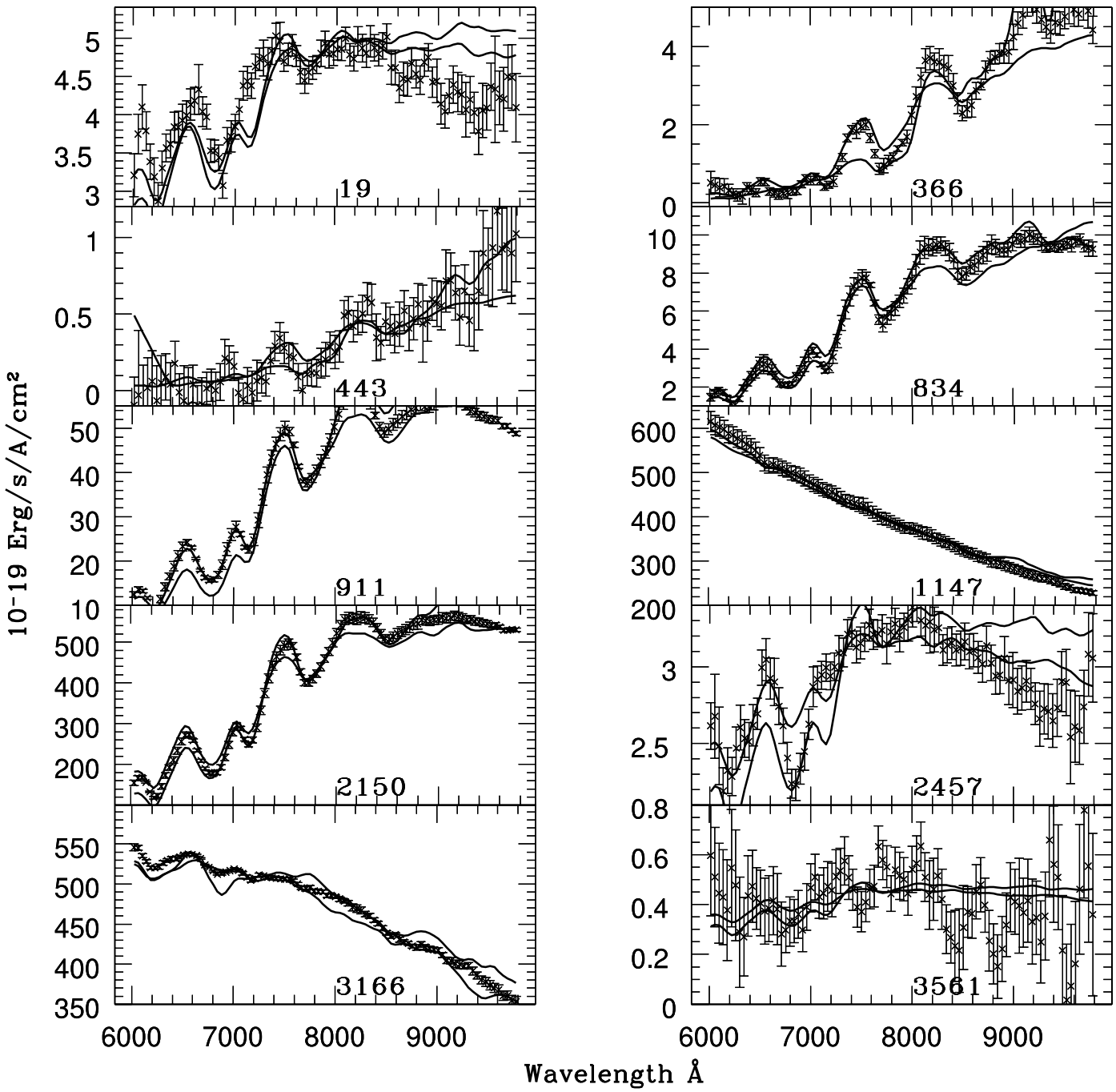

FIG. 3.—GRAPES spectra of unresolved objects 19, 366, 443, 834, 911, 1147, 2150, 2457, 3166, and 3561 in the HUDF and the two best-matching templates (*solid lines*) listed in Table 2.

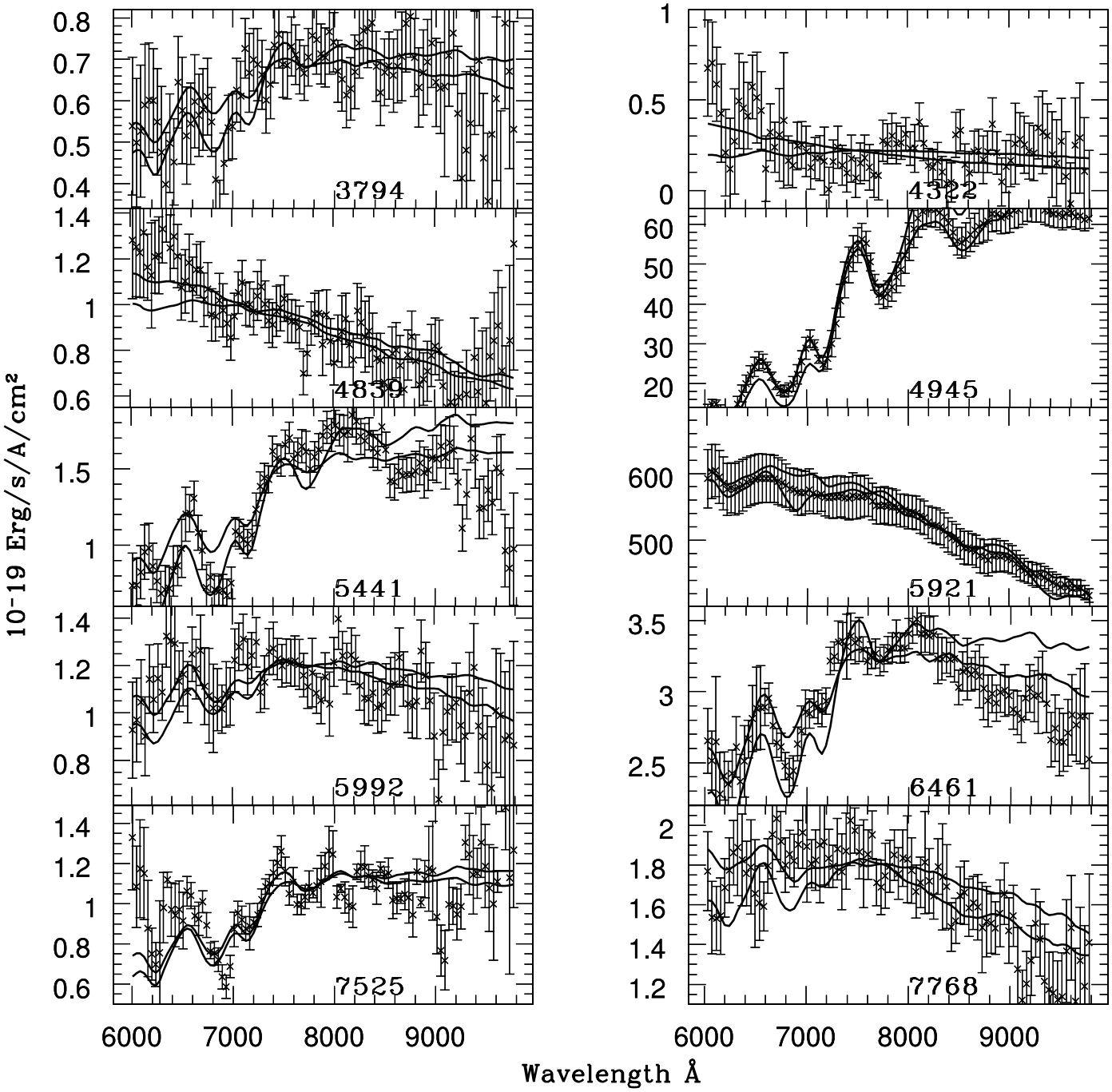

FIG. 4.—Same as Fig. 3, but for objects 3794, 4322, 4839, 4945, 5441, 5921, 5992, 6461, 7525, and 7768.

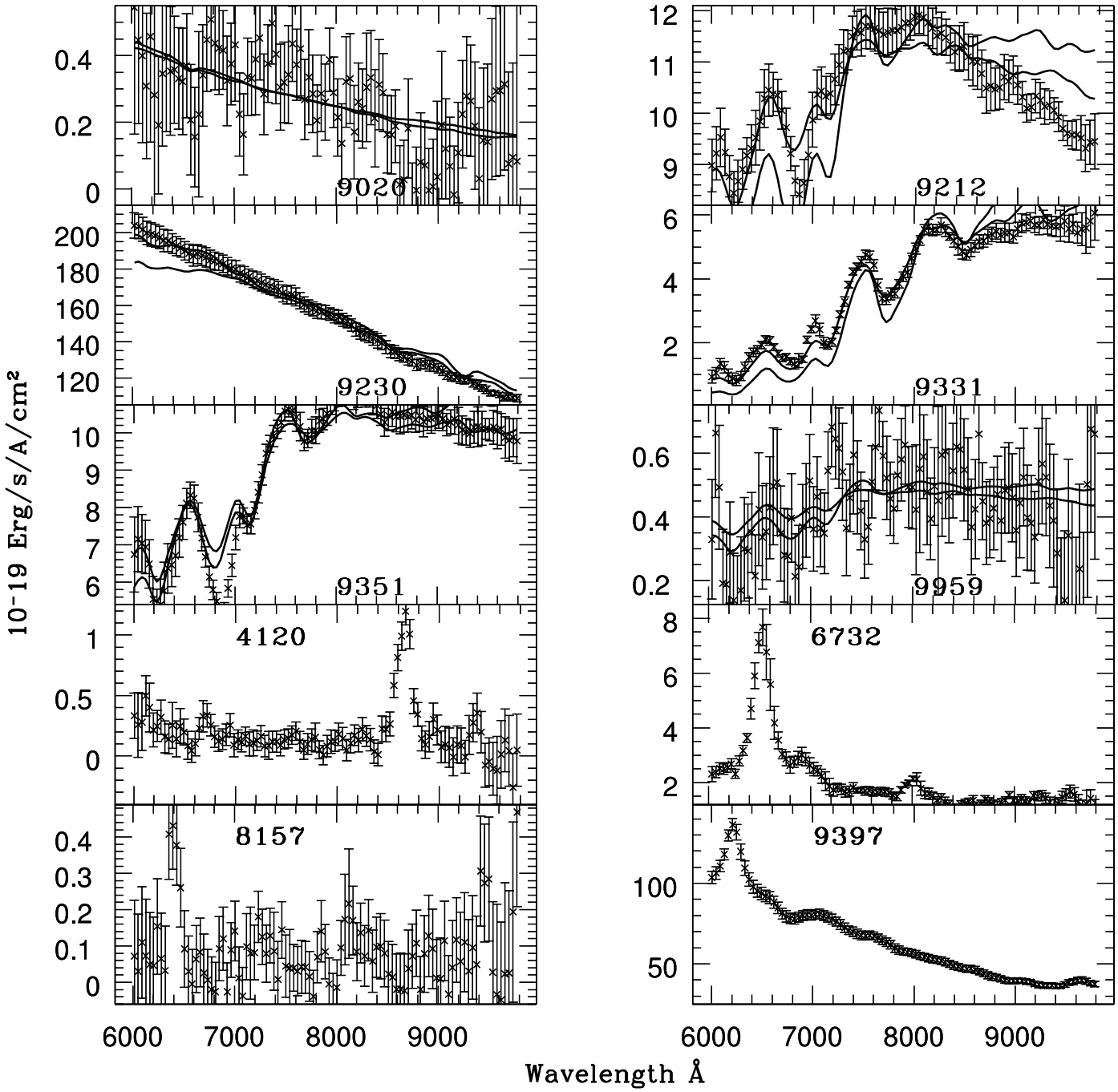

FIG. 5.—Same as Fig. 3, but for objects 9020, 9212, 9230, 9331, 9351, and 9959. The bottom four objects are the extragalactic sources 4120, 6732, 8157, and 9397, estimated to be at redshifts of $z = 2.1$, $z = 3.2$, $z \geq 3.0$, and $z = 3.0$, respectively (C. Xu et al. 2005, in preparation).

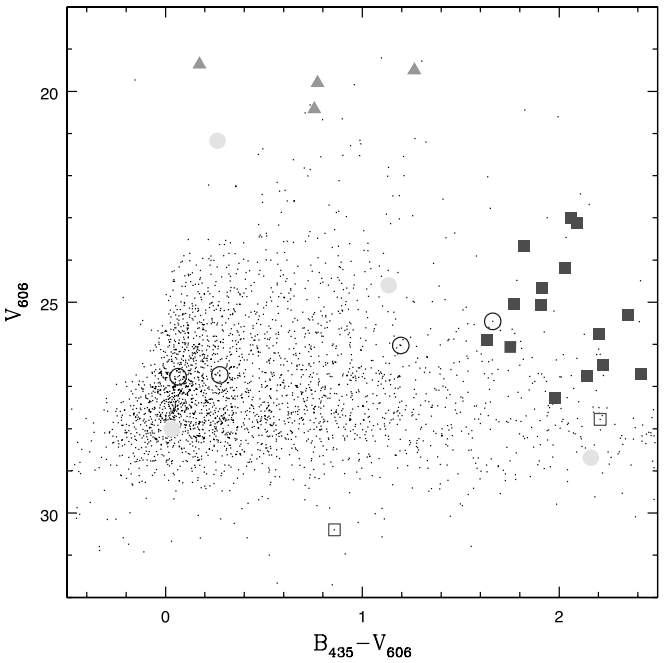

FIG. 6.—Location of the 28 spectroscopically identified sources in a magnitude-color plot (V_{606} vs. $B_{435} - V_{606}$). The small black points are the entire set of objects in the HUDF catalog with $i_{775} \leq 29.0$ mag and $z_{850} \leq 28.2$ mag. Filled dark gray squares are M dwarfs. Open dark gray squares are the two L dwarf candidates. Filled medium gray triangles represent the non-M or L dwarf stars, which could be main-sequence stars. Open black circles are white dwarf candidates (Table 3). Filled light gray circles represent the QSOs. [*See the electronic edition of the Journal for a color version of this figure*.]

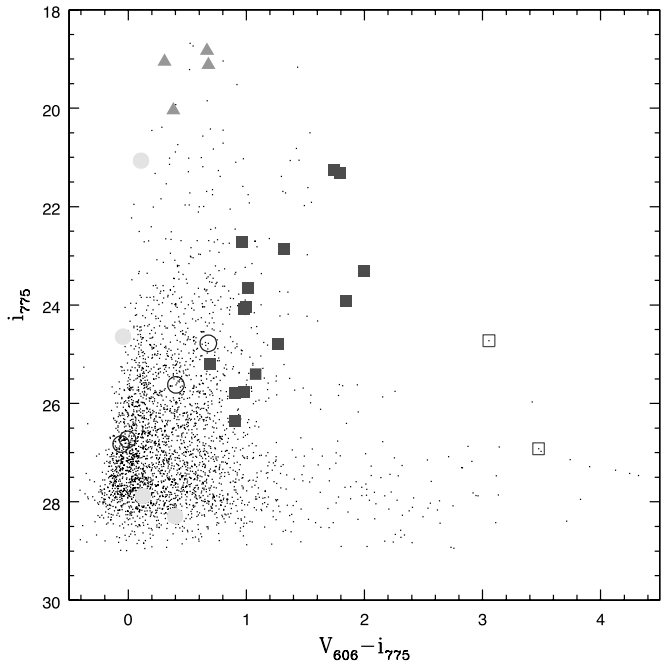

FIG. 7.—Same as Fig. 6, but for i_{775} vs. $V_{606} - i_{775}$. [*See the electronic edition of the Journal for a color version of this figure*.]

the velocity expected for an object that is in the Galactic disk (i.e., $\geq$100 km s^{-1}; Chiba & Beers 2000).

The HUDF image stacks (§ 2) were subtracted from one another and the results were examined to see whether any object, whether classified as extended or not on the basis of its $S_{z_{850}}$ value, had moved significantly (e.g., more than 2.5 HUDF pixels) from one image to the next. No such object was found.

The motion of objects in the HUDF was further investigated by carefully measuring the position of objects separately in each of the eight available i_{775}-band HUDF partial image stacks. These positions were measured using the IDL task MPFIT2DPEAK,[7] using a fixed-width (FWHM = 2.5 pixels) Gaussian fit. Initially, the positions of the 360 most compact sources ($S \leq 0.1$ and $i_{775} \leq 28.5$ mag) were examined. An average position and a standard deviation of the mean were computed for each object in the field using epoch 1 and epoch 2 HUDF image stacks separately. Average epoch 1 and epoch 2 positions were subtracted from one another to compute the observed shift of each object. These are shown (scaled up by a factor of 500) in Figure 8 (*left*). Repeated measurements of the position of sources in the field using HUDF image stacks taken within the same epoch were always within 0.1 HUDF pixels, or 0.″003. Still, as shown in Figure 8, there is a systematic, field-dependent disagreement between the epoch 1 and epoch 2 measurements. This is likely caused by epoch 1 and epoch 2 images having been taken at position angles that are 90° apart, and/or the effect of telescope breathing, and/or a very small amount of residual image distortion that is not taken into account in the current model of the ACS distortion maps. To produce a 3 σ detection with these data, an object must have a measured proper motion larger than 0.54 HUDF pixels or $\mu \geq 0.''081$ yr^{-1}. No object in Table 1 was observed to have such a large proper motion.

The situation was improved using a simple third-order two-dimensional polynomial fit to the observed distribution shown in Figure 8 (*left*). This fit, when applied as a correction, results in significantly lower systematics across the field, as shown in Figure 8 (*right*). The accuracy of the corrected shifts (of compact objects) between epoch 1 and epoch 2 is improved by a factor of 3, with a 3 σ detection now corresponding to a shift of 0.18 HUDF pixels or $\mu \geq 0.''027$ yr^{-1}.

The search for high proper motion objects in the HUDF was extended to all 10,181 objects in the field by measuring and correcting (using the correction determined above) the observed shifts of these objects. Only four sources were found to have moved significantly (but with a significance slightly lower than 3 σ) from epoch 1 to epoch 2. These objects are UID 443, 9020, 911, and 7525, and they are all unresolved objects that are listed in Table 1. Their measured shifts are 0.17, 0.17, 0.14, and 0.15 HUDF pixels, respectively, or approximately 0.″02 yr^{-1}, which is smaller than our imposed 3 σ limit.

4.3. *Extragalactic Unresolved Sources*

Two unresolved, extragalactic sources with $i_{775} \leq 27.0$ were identified (UID 6732 and UID 9397). The GRAPES spectra of these objects show prominent emission lines, and the redshift of these objects is estimated to be $z = 3.2$ and 3.0, respectively (C. Xu et al. 2005, in preparation). Identification of such objects using GRAPES spectra could easily be carried out down to magnitudes fainter than $i_{775} = 27.0$ mag, as demonstrated by the fact that several fainter extragalactic objects with $27.0 \leq i_{775} \leq 29.5$ were easily identified (e.g., UID 4120 and UID 8157). Without spectral information, these objects would have been misidentified as stars (e.g., UID 9397 would be a good candidate for a cool white dwarf at a distance of $\approx$1 kpc). The issue of contamination by faint, blue extragalactic objects in previous studies (Ibata et al. 1999; Méndez & Minniti 2000) has been discussed in the past (Kilic et al. 2004), and Figures 6

[7] Available at http://astrog.physics.wisc.edu/~craigm/idl/.

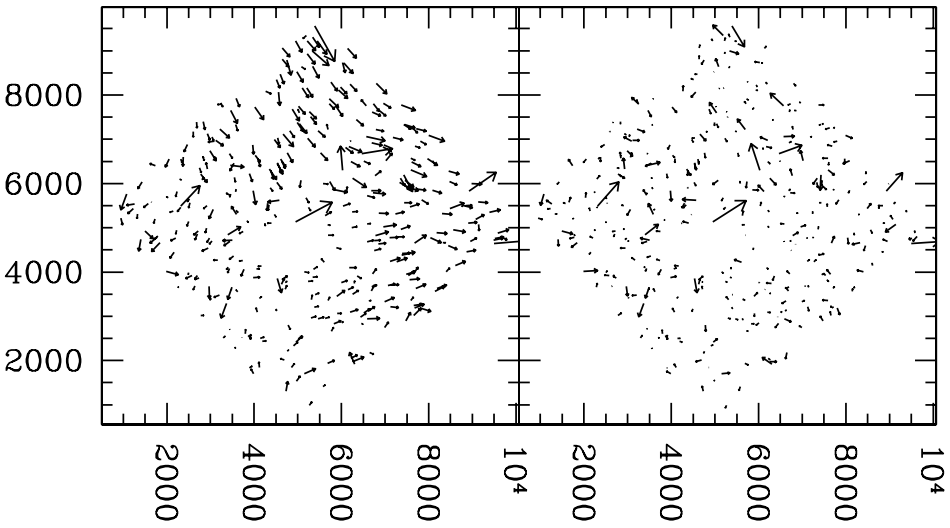

FIG. 8.—*Left*, Observed shifts (scaled by a factor of 500) of the 360 most compact sources in the HUDF between epoch 1 and epoch 2 i_{775}-band images; *right*, corrected shifts, obtained after applying a correction based on a fit of the raw measurements (see § 3.2). North is up. The axis units are HUDF pixels (0.″030 pixel^{-1}).

and 7 illustrate how these objects could be mistaken for a variety of stellar objects ranging from M and L dwarfs to white dwarfs. Spectroscopic confirmation is therefore crucial to accurately determine stellar counts in deep fields such as the HUDF. There are two extragalactic objects among the 28 point sources with $i_{775} \leq 27.0$ mag, which corresponds to a 7% contamination level at these Galactic coordinates.

The two extragalactic objects (UID 6732 and UID 9397) were used to check the accuracy of the proper-motion measurements described in § 3.2. The measured shifts of these objects between epoch 1 and epoch 2 are smaller than 0.04 HUDF pixels (0.″0012), which is what one would expect on the basis of the proper-motion error estimate quoted in § 3.2.

There are a total of 14 faint ($27.0 \leq i_{775} \leq 29.5$), blue ($B_{435} - V_{606} \leq 1.8$, $V_{606} - i_{775} \leq 0.8$) objects listed in Table 1 that were not included in the analysis above because they are either too faint to have usable GRAPES spectra or robust *S*-based classifications. Some of these sources might well be faint white dwarfs in either the Galactic disk or halo but are hard to distinguish from extragalactic sources without higher signal-to-noise ratio spectra or more accurate proper-motion measurements.

5. DISCUSSION

5.1. *M and L Dwarfs and the Galactic Disk Scale Height*

Eighteen objects were identified as M (or early L) dwarf main-sequence stars. Two objects were best fitted by early L dwarf templates (Kirkpatrick et al. 2000). Both of these objects are red enough to be outside of the color range shown in Figures 9 and 10, with $V_{606} - i_{775} = 2.21$ and 3.47. Deep infrared observations of these two objects will be required to confirm that they are L dwarfs. NICMOS observations of the HUDF did not detect these objects in either the *J* or *H* bands. All other very red objects are best fitted using M dwarf templates. The broad spectral features of M dwarfs listed in Table 2 were well fitted using M dwarf Pickles (1998) templates, and for objects brighter than $i_{775} = 27.0$ mag, we believe the identification to be secure.

Because these late-type sources can be seen to great distances, they can be used to probe the structure of the Galactic disk and halo as traced by the lowest mass stellar components of these populations. This was explored using Monte Carlo mass function (MF) simulations based on those developed by Burgasser (2004). Assuming power-law representations of the MF, $dN/dM \propto M^{-\alpha}$, for masses 0.005–0.2 $M_\odot$, luminosity function (LF) and effective temperature ($T_{\rm eff}$) distributions were created using evolutionary models from Burrows et al. (1997) over the range 100 K $\lesssim T_{\rm eff} \lesssim$ 4000 K. For all simulations, α was fixed at 1.13 for 0.1 $M_\odot \lesssim M \lesssim$ 0.2 $M_\odot$ (Reid et al. 1999) but allowed to vary between 0.5 and 1.5 for $M \lesssim 0.1$ $M_\odot$;

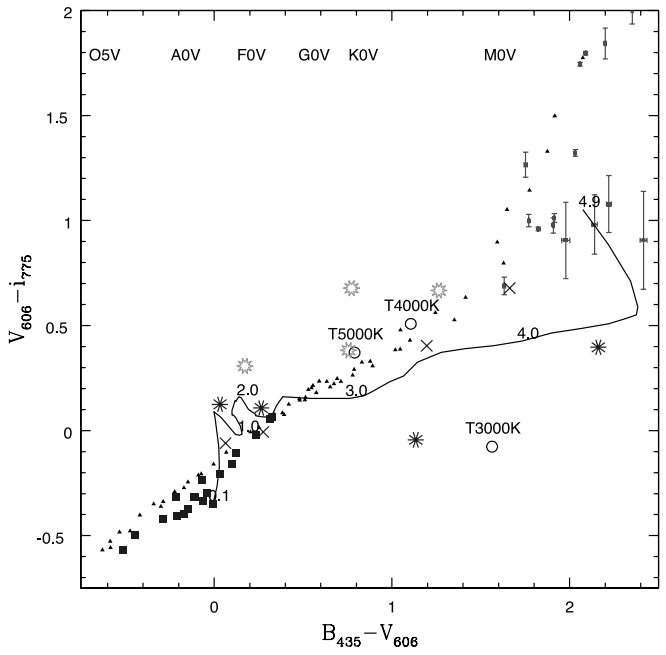

FIG. 9.—Color-color ($V_{606} - i_{775}$ vs. $B_{435} - V_{606}$) plot showing $i_{775} \leq 27.0$, unresolved, spectroscopically identified objects in the HUDF. M and L dwarfs are shown using medium gray squares with photometric error bars. Main-sequence stars are shown in light gray sunburst circles. Extragalactic objects, including those dimmer than $i_{775} = 27.0$ mag, are shown using large dark gray asterisks. The five white dwarf candidates are shown using large dark gray crosses. Pickles main-sequence objects are also shown using small black triangles. The $B_{435} - V_{606}$ locations of the O, A, F, G, K, and M stellar types are shown for reference. Hot white dwarfs are shown in large dark gray squares. Cool white dwarfs (3000, 4000, and 5000 K; Harris et al. 2001) are shown using labeled open circles. Finally, the solid black line shows the QSO track from a redshift of $z = 4.9$ (*top right*) to 0.1 (*bottom left*). [*See the electronic edition of the Journal for a color version of this figure*.]

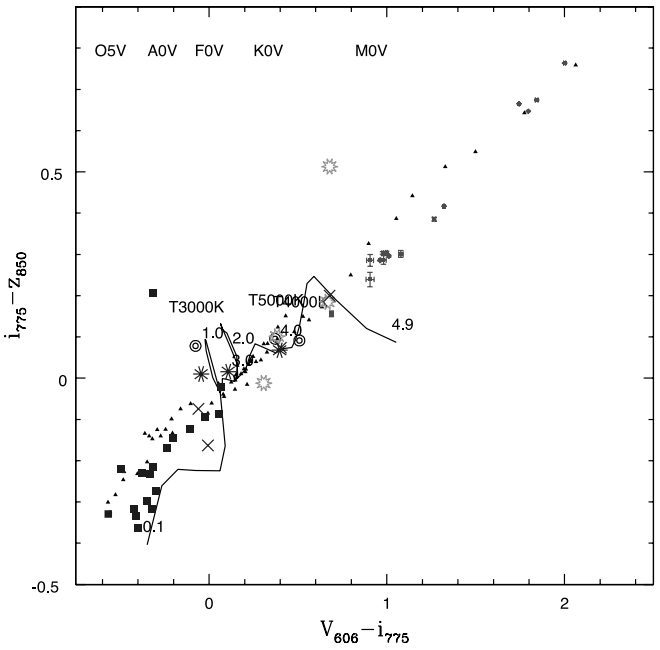

FIG. 10.—Same as Fig. 9, but for $i_{775} - z_{850}$ vs. $V_{606} - i_{775}$. [*See the electronic edition of the Journal for a color version of this figure*.]

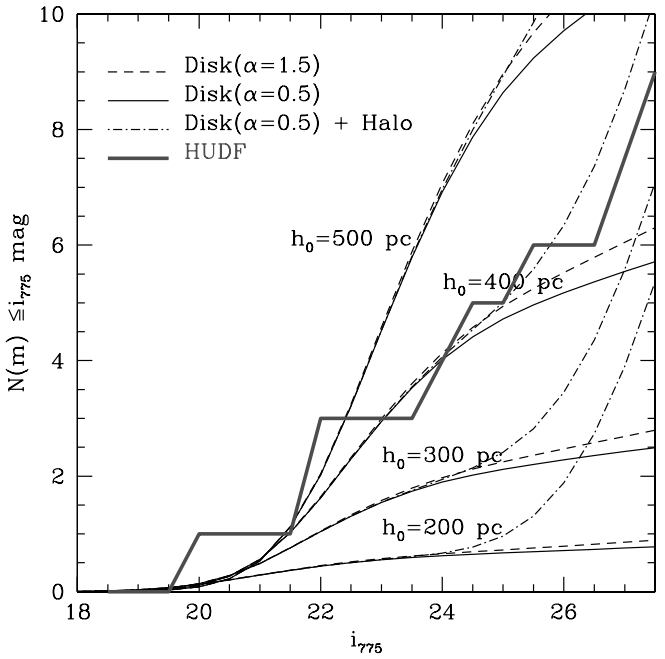

FIG. 11.—Predicted and observed cumulative luminosity functions of stars with spectral types M4 and later. This plot shows the expected distribution from the Galactic disk and halo. Four different disk scale heights are plotted with h_0 values of 200, 300, 400, and 500 pc (*bottom curves to top curves, respectively*). For each value of h_0, MFs corresponding to $\alpha = 0.5$ and 1.5 are shown (*solid and dashed lines, respectively*). The observed HUDF distribution is shown using a solid dark gray line, which is best fitted by a disk with a scale height of $h_0 = 400$ pc while reasonably excluding values of $h_0 = 200$, 300, and 500. [*See the electronic edition of the Journal for a color version of this figure*.]

number densities are normalized to the empirical value at 0.1 $M_\odot$ from the 8 pc sample (Reid et al. 1999).

Two separate populations were simulated: a disk population with a flat age distribution spanning 10 Myr to 10 Gyr (the majority of sources have age greater than 1 Gyr), and a halo population with uniformly sampled ages between 9 and 10 Gyr and a relative number density of 0.25% (Digby et al. 2003). The resulting bolometric LFs were converted to I (Cousins) LFs using a polynomial fit to empirical data (spanning $12.4 \lesssim M_i \lesssim 22.2$; i.e., M4 to T8) from Dahn et al. (2002) and Golimowski et al. (2004). Note that this fit is based on measurements for solar-metallicity field dwarfs and may not be appropriate for a subsolar-metallicity halo subdwarf population. Apparent I-band distributions were determined by first assuming a constant density population out to a limiting magnitude $m_I = 27.5$ (taking into account the difference between HUDF AB magnitudes and Vega magnitudes from the empirical data) and then applying a correction for the vertical distribution of sources. For the disk population, we assumed a density distribution $n \propto \mathrm{sech}(z/h_0)^2$ (Reid & Hawley 2000), where $z = d\sin\beta$, d is the source distance, $\beta = 54.^\circ5$ is the Galactic latitude of the HUDF, and h_0 is the $1/e$ disk scale height, assumed to range between 200 and 500 pc. For the halo population, a galactocentric oblate spheroid distribution as given in Digby et al. (2003) was assumed, using the values derived there and an axial ratio $q = c/a = 0.7$.

Figure 11 presents the results of these simulations in the form of cumulative number distributions as a function of i_{775} magnitude down to the limiting magnitude of our sample. These distributions show that variations in the disk scale height are far more pronounced than those from the different MFs assumed, and this analysis is limited to the former parameter. The cumulative distribution of the six dwarfs in Table 2 with spectral types M4 and later (consistent with the mass constraints of the simulations) is also shown. The observed distribution matches that of the $h_0 = 400$ pc disk simulation very well, particularly out to $i_{775} \lesssim 23.5$ mag, where the halo population makes a negligible contribution. Because the simulated distributions are rather sensitive to the disk scale height, particularly at fainter apparent magnitudes, one can conservatively constrain h_0 to ± 100 pc assuming Poisson uncertainties. This is in good agreement with the estimate of 340 ± 84 pc from R. Ryan et al. (2005, in preparation), which was computed using ACS HUDF parallel fields i-band dropout galaxies. For $i_{775} \geq 25$ mag, the observed distribution is slightly greater than the disk population alone but does not increase as sharply as the combined disk +halo distribution. Indeed, the shape of the observed number distribution implies few, if any, halo stars in the HUDF down to $i_{775} = 27.0$ mag, consistent with the lack of significant proper motion sources in this sample. This suggests that either the number density ratio of halo to disk stars or the adopted axial ratio for the halo density distribution, or both, may be smaller than assumed here. With no late-type halo subdwarf detections in this sample, we cannot usefully constrain these possibilities.

5.2. *White Dwarfs*

5.2.1. *White Dwarf Candidates*

Objects brighter than $i_{775} = 27.0$ were individually examined, and distances were estimated under various assumptions of what the exact nature of each object might be: (1) a main-sequence star, (2) a young white dwarf, or (3) an old white dwarf. The reddest objects, which are all well fitted by M and later type templates, as well as the few extragalactic objects identified in § 4.3, were excluded from this analysis. The remaining eight objects were all initially considered to be potential white dwarfs.

Assuming that an object is a white dwarf, one can use the measured $V_{606} - i_{775}$ color of that object (Table 1) and the cooling curves of Richer et al. (2000) (after accounting for passband and zero-point differences) to derive an absolute V_{606}-band magnitude, an age, and a distance to that object. As shown in

TABLE 3
WHITE DWARF CANDIDATES IN THE HUDF

UID	Type	$M_{V_{606}}$	D (pc)	Age (Gyr)	$V_{T\,\max}$ (km s^{-1})	Possible Type	$1/V_{\max}$ (stars pc^{-3})
1147	MS F6–F8	3.7–4.0	$(1.5 \pm 1.1) \times 10^4$	...	...	F6–F8	...
	Young WD	14.0–15.0	110 ± 24	1.4–3.9	14.1	...	...
	Old WD	17.4–18.3	24 ± 5	10.3–12.1	3.0	...	...
3166	MS K4–K5	6.8–7.1	$(3.7 \pm 0.23) \times 10^3$	...	...	K4–K5	...
	Young WD	14.8–15.8	80 ± 18	2.5–5.7	10.2	...	...
	Old WD	17.2–18.2	27 ± 6	9.9–11.5	3.5	...	...
4322	MS A7–K5	2.3–7.1	$(4.29 \pm 3.4) \times 10^5$	...	...	...	...
	Young WD	12.1–13.1	$(6.9 \pm 1.6) \times 10^3$	0.4–1.4	1545.6	...	...
	Old WD	17.5–18.4	590 ± 126	10.7–12.9	75.5	Disk or halo	3.37×10^{-3}
4839	MS G5–K2	5.0–6.3	$(1.2 \pm 0.3) \times 10^5$	...	...	...	...
	Young WD	12.5–13.5	$(2.4 \pm 0.5) \times 10^3$	1.1–3.3	885.0	Disk	9.45×10^{-6}
	Old WD	17.4–18.3	417 ± 88	10.4–12.3	53.4	Disk or halo	1.80×10^{-2}
5921	MS K4–K5	6.8–7.1	$(3.7 \pm 0.2) \times 10^3$	...	...	K4–K5	...
	Young WD	14.5–15.5	93 ± 20	1.9–4.7	11.9	...	...
	Old WD	17.3–18.2	26 ± 5	10.1–11.7	3.3	...	...
7768	MS K5–K7	7.1–7.6	$(4.1 \pm 0.5) \times 10^4$	...	...	...	...
	Young WD	14.5–15.5	$(1.3 \pm 0.3) \times 10^3$	1.9–4.7	160.2	Disk	2.1×10^{-5}
	Old WD	17.3–18.2	345 ± 70	10.1–11.7	44.1	Disk or halo	9.9×10^{-4}
9020	MS F0–F2	2.7–3.6	$(5.2 \pm 1.0) \times 10^5$	...	...	...	...
	Young WD	13.3–13.3	$(6.2 \pm 1.4) \times 10^3$	0.5–1.6	793.9	...	...
	Old WD	17.5–18.4	576 ± 123	10.7–12.9	73.7	Disk or halo	3.16×10^{-3}
9230	MS K2–K3	6.3–6.7	$(6.3 \pm 0.4) \times 10^3$	...	...	K2–K3	...
	Young WD	13.6–14.6	187 ± 41	1.1–3.2	23.9	...	...
	Old WD	17.5–18.4	32 ± 7	10.4–12.3	4.0	...	...

NOTES.—All objects have $i_{775} \leq 27.0$ mag. We list the derived distance to each object under the assumption that it is a main-sequence star or white dwarf (Richer et al. 2000) with the appropriate $V-i$ colors (see Table 1). The value $V_{T\,\max}$ is the upper limit of the tangential velocity (V_T) of each object. The seventh column lists the acceptable nature of the object, and the last column gives the $1/V_{\max}$ density for that particular object and scenario. Section 5.2 explains how these quantities were derived in more detail.

Figure 2 of Richer et al. (2000), blue white dwarfs can either be young, hot objects (age $\leq$ 5 Gyr, $T \approx 10^4$ K, $M_{V_{606}} \leq 16.0$ mag) or older, cooler, intrinsically dimmer ones (age $\geq$ 10 Gyr, $T \approx 3 \times 10^3$ K, $M_{V_{606}} \geq 16.0$ mag). This results in several white dwarf distance estimates for each object.

Proceeding via a process of elimination, the distinction between main-sequence stars, young white dwarfs, old white dwarfs, and disk or halo white dwarfs is possible. Assuming that a star is a main-sequence star, which is intrinsically much more luminous than a white dwarf, can cause the distance estimate for that object to be unreasonably large. Assuming that a star is a young white dwarf (age $\leq$ 5.0 Gyr) implies that this object is less likely to be part of the Galactic halo, since the latter is composed of much older objects. In addition, on the basis of the lack of proper motion detection discussed in § 4.2, one can define an upper limit to the tangential velocity ($V_{T_{\max}}$) of each object once its distance is determined. The motion of an object moving by more than 0.18 HUDF pixels (0.″027 yr^{-1}) should have been detected at the 3 σ significance level, as discussed in § 3.2. As discussed above, objects in the Galactic halo are expected to have velocities around 100–200 km s^{-1}. Even if projection effects result in lower values of V_T, one would expect at least some of them to have V_T values larger than 30–60 km s^{-1}. A final clue to help narrow down the nature of a particular object is provided by the fact that an object that is nearby would suffer from a significant, easily measurable, parallax during the 73 day interval between epoch 1 and epoch 2 observations. Calculating the parallax vector for the HUDF exposures shows that an object 30 pc away would produce a parallax of about 0.″060, or 2 HUDF pixels, between epoch 1 and epoch 2 observations. Objects that are closer than 200 pc are therefore expected to produce a parallax that would be detected at more than a 3 σ level.

Examining Table 3, objects 4322, 4839, 7768, and 9020 are unlikely to be main-sequence stars, as this would make them very distant objects. The Magellanic Stream (Mathewson & Ford 1984) is too far away from the HUDF to possibly explain the existence of main-sequence stars at such large distances. Objects 1147, 3166, and 5921, which do not (this is true of all objects listed in Table 3) have measurable parallax or proper motion, are not likely to be white dwarfs. Being either young or old white dwarfs would place these two objects less than 200 pc away and would have resulted in measurable parallax in the HUDF image stacks. Another object unlikely to be a white dwarf is object 9230, which was observed to have a fainter, unresolved companion 0.″5 away. This companion, for which we have no GRAPES spectrum, has a V_{606}-band magnitude of $V_{606} = 23.7$ mag and the colors $B_{435} - V_{606} = 1.6$, $V_{606} - i_{775} = 0.9$, and $i_{775} - z_{850} = 0.4$ mag. On the basis of these colors, this object should be an early M dwarf that is $(4.9 \pm 1.2) \times 10^3$ pc away. This places both object 9230 and its companion at the same distance (within error bars). The likelihood of any two stars being within 0.″5 in the HUDF and at nearly the same distance is very small ($\leq 5 \times 10^{-3}$), and these two objects are likely to be part of a binary system, with object 9230 being a K-type main-sequence star. Independently of this, object 9230 cannot be an old white dwarf, since this would place this object at a distance of 34 pc, where its parallax motion would have been very easily detected.

5.2.2. *Disk or Halo White Dwarfs?*

Four objects (4322, 4839, 7768, and 9020) remain as white dwarf candidates. Using a simple $1/V_{\max}$ (Schmidt 1968; Tinney

et al. 1993; Méndez 2002) analysis, the white dwarf number density in the direction of the HUDF can be computed. The detection of four white dwarfs in the HUDF implies a local density of between $(3.5 \pm 1.5) \times 10^{-5}$ and $(1.1 \pm 0.3) \times 10^{-2}$ stars pc^{-3}. The upper and lower limits on the density are computed using old or young white dwarfs, respectively, whereas the errors reflect the large uncertainties in the intrinsic luminosities of young and old white dwarfs ($\sim$1.0 mag). Note that this estimate is actually not affected by whether or not object 9230 was included as an HUDF white dwarf. The contribution of this object to the $1/V_{\max}$ value is negligible. For comparison, Liebert et al. (1988) determined the local white dwarf density to be 3.0×10^{-3} stars pc^{-3}, whereas Reid et al. (2001) found a value of $(3.26 \pm 1.23) \times 10^{-3}$ stars pc^{-3} and Méndez (2002) derived a density of white dwarfs in the thick disk of $(2.610 \pm 0.59) \times 10^{-2}$ stars pc^{-3}. The white dwarf density derived here is consistent with most of the previous density estimates. Properly determining the disk and halo membership of the four white dwarfs identified in the HUDF will be needed before a stronger conclusion can be made. Reobserving the HUDF field in the i_{775} band in 1.5 yr would allow (assuming that a 0.18 HUDF pixel shift corresponds to a 3 σ level detection) one to unambiguously detect the proper motion of halo white dwarfs with $V_T \geq 100$ km s^{-1} at distances up to 1000 pc.

The above density estimate assumed that all four HUDF white dwarfs were Galactic disk objects. Could some of these objects be in the Galactic halo? At least two of these objects (UID 4839 and UID 7768) have $V_{T_{\max}}$ values that are lower than 60 km s^{-1}. The probability that this is caused by a projection effect is under 10% (assuming a relatively low velocity of $\approx$100 km s^{-1} for halo objects). The last two white dwarfs listed in Table 3 (4322 and 9020) are at slightly larger distances, which average to 583 pc, and more importantly have larger values of $V_{T_{\max}}$. The average distance of these objects still seems a bit low for objects that would be part of a Galactic halo whose density increases all the way up to 7 kpc (Reid & Majewski 1993), whereas white dwarfs with absolute magnitudes of $M_{V_{606}} = 17$ mag (Harris et al. 2003) should be detected all the way out to 1000 pc. Unless these objects are intrinsically much dimmer, one would expect the average distance to these two objects to be larger than 583 pc and much closer to our limit of 1000 pc. The $V_{T_{\max}}$ values inferred for objects 4322 and 9020, although higher than those of objects 4839 and 7768, fall substantially short of expected typical halo velocities. The probability of observing each of the objects with the $V_{T_{\max}}$ values listed in Table 3 is between 14% and 20%. As a group, the probability that objects 4322 and 9020 are halo objects is under 3%. Similarly, the hypothesis that all four detected white dwarfs in the HUDF are halo rather than disk objects is excluded at the 99.9986% level. Overall, the distances to the four white dwarf candidates identified here is more consistent with them being part of a Galactic thick disk. Majewski & Siegel (2002) derived a disk scale height of 400–600 pc using a study of low-velocity white dwarfs. This value was somewhat larger than previous estimates of 250–350 pc, but it is interesting to note that the M dwarf disk scale height derived in § 5.1, as well as the distance estimates of the white dwarfs listed in Table 3, all appear to agree with this value.

It would be interesting to attempt to set an upper limit on the halo white dwarf density on the basis of the finding of up to two white dwarfs in the HUDF. Under this assumption, the upper limit to the Galactic halo white dwarf density is computed to be $(6.53 \pm 3) \times 10^{-3}$ stars pc^{-3}. This result is consistent with the previous work of Méndez & Minniti (2000) using the combined observations of the Hubble Deep Fields North and South (7.73×10^{-3} stars pc^{-3}).

A Population II halo white dwarf population that is older than 12–13 Gyr would have remained undetected here. (An intrinsically fainter than $M_{V_{606}} = 17.0$ mag white dwarf population would also help explaining the low average distances of the white dwarfs listed in Table 3.) As discussed above, the white dwarfs identified in this work are more likely to be within the Galactic thick disk. It is to be noted that Kilic et al. (2004) recently observed a disproportionately large ratio of disk to halo white dwarfs in the Hubble Deep Field North. Kilic et al. (2004) found no evidence of any white dwarfs with tangential velocities larger than 30 km s^{-1} down to $i_{775} = 27.5$ mag, and the authors concluded that the blue objects they saw were all part of the Galactic disk. Similarly, the HUDF observations presented here successfully identified four white dwarf candidates with $i_{775} \leq 27.0$ mag in the HUDF, none very likely to be in the Galactic halo, where 2–3 σ detection would have been expected to be consistent with previous studies.

5.2.3. *Dark Matter Halo White Dwarfs?*

Although dynamical studies of the Galaxy predict the dark matter white dwarf density to be as high as 1.26×10^{-2} stars pc^{-3} (assuming that 100% of the dark matter halo mass is in the form of 0.6 $M_\odot$ white dwarfs), the failure to detect a significant population of high-velocity white dwarfs in the HUDF points to a dark matter halo devoid of a significant white dwarf population. Following the methodology of Kawaler (1996), one can estimate the amount of dark matter halo mass that is probed by the HUDF images and directly compute the fraction of the dark matter halo mass that could be contained in a white dwarf population. Assuming a white dwarf absolute $M_{i_{775}}$ magnitude of 17.0 mag (Harris et al. 2003) and a limiting magnitude of $i_{775} = 27.0$ mag, the maximum probed distance is 1000 pc. In the corresponding volume and in the direction of the HUDF, the included dark matter halo mass is 3 $M_\odot$. A population of dark matter halo white dwarfs could have remained undetected in this study for several reasons. (1) The method used in this paper may be inefficient at properly identifying halo white dwarfs in Table 3. In this case, if one assumes that the HUDF contains four halo white dwarfs ($i_{775} \leq 27.0$), these would account for 2 $M_\odot$, a significant fraction of the expected dark matter halo mass. This would, however, increase the ratio of halo to disk white dwarfs to unrealistically high levels (i.e., $\gg$2%) and would assume that all the white dwarfs seen in the HUDF are from the dark matter halo and not from the Population II halo, which is highly unrealistic. The lack of proper-motion detections also makes this scenario unlikely. (2) White dwarfs do not contribute significantly to the Galactic dark matter halo mass. From microlensing experiments toward the Magellanic Clouds, the contribution of MACHO objects to dark matter has been estimated to be anywhere from 20% to less than 2% (Alcock et al. 2000; Afonso et al. 2003; Sahu 2003; Evans & Belokurov 2005 and references therein). Furthermore, Majewski & Siegel (2002) showed how an increased thick disk scale height of 400–600 pc makes it unlikely that white dwarfs could be the MACHO objects. (3) White dwarfs could contribute significantly to the mass of the Galactic dark matter halo but are too faint to be detected in this study. Richer et al. (2000) showed that an increase in the age of the white dwarf halo population from 10 to 16 Gyr is expected to reduce the number of white dwarf detections (down to $V_{606} = 28.0$) by a factor of 7. The lack of high-velocity white dwarf detections in the HUDF puts upper limits on the contribution of a hypothetical white dwarf population to

the Galactic dark matter halo. Based on the brightest objects in the HUDF for which we have spectra (i.e., $i_{775} \leq 27.0$), if the dark matter halo is as old as about 12 Gyr (Hansen et al. 2002; Chaboyer et al. 1998), then dark matter halo white dwarfs with $M_V = 17.5$ ($M_{i_{775}} = 17.0$) contribute less than 20% to the dark matter. If the age of the dark matter halo is 10 Gyr, white dwarfs ($M_{i_{775}} = 15.9$) contribute less than 2% to the dark matter.

The possibility that there is a large population of faint white dwarfs that has remained unidentified in this study and that would account for a significant fraction of the dark matter halo can be investigated a little further. Recall that in § 4.3, 14 sources with $27.0 \leq i_{775} \leq 29.5$ and blue ($B_{435} - V_{606} \leq 1.8$, $V_{606} - i_{775} \leq 0.8$) colors were identified. Not all of these sources were expected to be bona fide stars, and some are likely to be extragalactic sources, but as discussed in § 3.1, it is estimated that 95% of the stars in the HUDF were properly identified, so this number should be considered an upper limit on the number of faint stars in the HUDF. Following the same methodology used above, but now using a limiting magnitude of $i_{775} \leq 29.5$, the HUDF images probe through 79 $M_\odot$ of the dark matter halo. Even under the extreme assumption that all 14 unresolved candidates in the HUDF are high-velocity white dwarfs, this implies that, when reaching down to $i_{775} = 29.5$, faint white dwarfs in the Galactic dark matter halo contribute less than 10% to the total dark matter halo mass for a dark matter halo age of 12 Gyr. Future observations of the HUDF would allow more sensitive measurements of the proper motion of these faint objects (§ 5.2.2). Setting tighter constraints on the maximum tangential velocities of these faint HUDF unresolved objects would allow us to exclude some of these objects from the high-velocity white dwarfs and would allow us to further lower the maximum fraction of the dark matter halo mass that could be accounted for by white dwarfs.

6. CONCLUSIONS

A systematic search for unresolved objects in the HUDF identified 46 objects with $i_{775} \leq 29.5$ mag. Using the GRAPES spectra of these objects, 28 objects with $i_{775} \leq 27.0$ mag were spectroscopically identified, including 18 M and later dwarfs (including two unconfirmed L dwarf candidates) and 2 QSOs. The M dwarf luminosity function of M4 and later type stars was computed and compared with predictions based on Monte Carlo simulations. If we assume a simple analytical model of the Galactic disk, the number of detected M dwarfs was shown to be large enough to constrain the scale height of the M and L dwarf Galactic disk to $h_0 = 400 \pm 100$ pc. Out of eight stars that were found not to be M or later type stars, four stars were determined to be old white dwarf candidates. Not a single object was found to have a proper motion that is larger than $0''.027$ yr^{-1}, making them likely Galactic thick disk objects. Further imaging of the HUDF using a time span larger than 1.5 yr would provide more sensitive proper-motion measurements. More sensitive proper-motion measurements are required to positively place unresolved objects in the Galactic disk or halo. It would also allow us to search for high tangential velocity objects among the 14 fainter ($27.0 \leq i_{775} \leq 29.5$) unresolved sources identified in the HUDF. Excluding halo membership of objects down to $i_{775} = 29.5$ on the basis of proper-motion measurements would further constrain the maximum white dwarf contribution to the dark matter halo mass. The currently available observations of the HUDF, spanning 73 days, show the absence of a significant population of high-velocity white dwarfs down to $i_{775} = 27.0$ and a relatively small number of unresolved, faint blue sources in the field down to $i_{775} = 29.5$. This is interpreted as a consequence of white dwarfs accounting for less than 10% of the dark matter halo, if we assume that the dark matter halo is 12 Gyr old.

We would like to thank I. N. Reid for helpful discussions. This work was supported by grant GO 09793.01-A from the Space Telescope Science Institute, which is operated by the Association of Universities for Research in Astronomy, Inc., under NASA contract NAS5-26555.

REFERENCES

Afonso, C., et al. 2003, A&A, 404, 145
Alcock, C., et al. 2000, ApJ, 542, 281
Allen, C. W. 2000, Allen's Astrophysical Quantities (4th ed.; London: Athlone Press)
Bertin, E., & Arnouts, S. 1996, A&AS, 117, 393
Burgasser, A. J. 2004, ApJS, 155, 191
Burgasser, A. J., Kirkpatrick, J. D., Liebert, J., & Burrows, A. 2003, ApJ, 594, 510
Burrows, A., et al. 1997, ApJ, 491, 856
Chaboyer, B., Demarque, P., Kernan, P. J., & Krauss, L. M. 1998, ApJ, 494, 96
Chiba, M., & Beers, T. C. 2000, AJ, 119, 2843
Dahn, C. C., et al. 2002, AJ, 124, 1170
Digby, A. P., Hambly, N. C., Cooke, J. A., Reid, I. N., & Cannon, R. D. 2003, MNRAS, 344, 583
Evans, N. W., & Belokurov, V. 2005, in Proc. 5th Int. Workshop on the Identification of Dark Matter, ed. N. J. C. Spooner & V. Kudryavtsev (Singapore: World Scientific), in press (astro-ph/0411222)
Fruchter, A. S., & Hook, R. N. 2002, PASP, 114, 144
Gates, I. E., & Gyuk, G. 2001, ApJ, 547, 786
Gates, I. E., et al. 2004, ApJ, 612, L129
Giavalisco, M., et al. 2004, ApJ, 600, L93
Golimowski, D. A., et al. 2004, AJ, 127, 3516
Hansen, B. M. S., et al. 2002, ApJ, 574, L155
Harris, H. C., et al. 2001, ApJ, 549, L109
———. 2003, AJ, 126, 1023
Ibata, R. A., Richer, H. B., Gilliland, R. L., & Scott, D. 1999, ApJ, 524, L95
Kawaler, S. D. 1996, ApJ, 467, L61
Kilic, M., von Hippel, T., Méndez, R. A., & Winget, D. E. 2004, ApJ, 609, 766
Kirkpatrick, J. D., et al. 2000, AJ, 120, 447
Liebert, J., Dahn, C. C., & Monet, D. G. 1988, ApJ, 332, 891
Majewski, S. R., & Siegel, M. H. 2002, ApJ, 569, 432
Mathewson, D. S., & Ford, V. L. 1984, in IAU Symp. 108, Structure and Evolution of the Magellanic Clouds, ed. S. van den Bergh & K. S. de Boer (Dordrecht: Reidel), 125
Méndez, R. A. 2002, A&A, 395, 779
Méndez, R. A., & Minniti, D. 2000, ApJ, 529, 911
Méndez, R. A., Minniti, D., De Marchi, G., Baker, A., & Couch, W. J. 1996, MNRAS, 283, 666
Oppenheimer, B. R., Hambly, N. C., Digby, A. P., Hodgkin, S. T., & Saumon, D. 2001, Science, 292, 698
Pickles, A. J. 1998, PASP, 110, 863
Pirzkal, N., et al. 2004, ApJS, 154, 501
Reid, I. N. 2005, ARA&A, in press
Reid, I. N., & Hawley, S. L. 2000, New Light on Dark Stars (Chichester: Praxis)
Reid, I. N., & Majewski, S. R. 1993, ApJ, 409, 635
Reid, I. N., Sahu, K. C., & Hawley, S. L. 2001, ApJ, 559, 942
Reid, I. N., et al. 1999, ApJ, 521, 613
Richer, H. B., Hansen, B., Limongi, M., Chieffi, A., Straniero, O., & Fahlman, G. C. 2000, ApJ, 529, 318
Sahu, K. C. 1994, Nature, 370, 275
———. 2003, in Proc. STScI Symp. (2001 April), The Dark Universe: Matter, Energy, and Gravity, ed. M. Livio (Cambridge: Cambridge Univ. Press), 14
Schlegel, D. J., Finkbeiner, D. P., & Davis, M. 1998, ApJ, 500, 525
Schmidt, M. 1968, ApJ, 151, 393
Tinney, C. G., Reid, I. N., & Mould, J. R. 1993, ApJ, 414, 254